Environmental Science & Technology

pubs.acs.org/est

Article

Defect-Rich Hierarchical Porous UiO-66(Zr) for Tunable Phosphate Removal

Mohua Li, Yanbiao Liu,* Fang Li, Chensi Shen, Yusuf Valentino Kaneti,* Yusuke Yamauchi, Brian Yuliarto, Bo Chen, and Chong-Chen Wang*

Cite This: *Environ. Sci. Technol.* 2021, 55, 13209−13218

Read Online

ACCESS | Metrics & More | Article Recommendations | Supporting Information

ABSTRACT: The introduction of defects into hierarchical porous metal−organic frameworks (HP-MOFs) is of vital significance to boost their adsorption performance. Herein, an advanced template-assisted strategy has been developed to fine-tune the phosphate adsorption performance of HP-MOFs by dictating the type and number of defects in HP-UiO-66(Zr). To achieve this, monocarboxylic acids of varying chain lengths have been employed as template molecules to fabricate an array of defect-rich HP-UiO-66(Zr) derivatives following removal of the template. The as-prepared HP-UiO-66(Zr) exhibits a higher sorption capacity and faster sorption rate compared to the pristine UiO-66(Zr). Particularly, the octanoic acid-modulated UiO-66(Zr) exhibits a high adsorption capacity of 186.6 mg P/g and an intraparticle diffusion rate of 6.19 mg/g·min$^{0.5}$, which are 4.8 times and 1.9 times higher than those of pristine UiO-66(Zr), respectively. The results reveal that defect sites play a critical role in boosting the phosphate uptake performance, which is further confirmed by various advanced characterizations. Density functional theory (DFT) calculations reveal the important role of defects in not only providing additional sorption sites but also reducing the sorption energy between HP-UiO-66(Zr) and phosphate. In addition, the hierarchical pores in HP-UiO-66(Zr) can accelerate the phosphate diffusion toward the active sorption sites. This work presents a promising route to tailor the adsorption performance of MOF-based adsorbents via defect engineering.

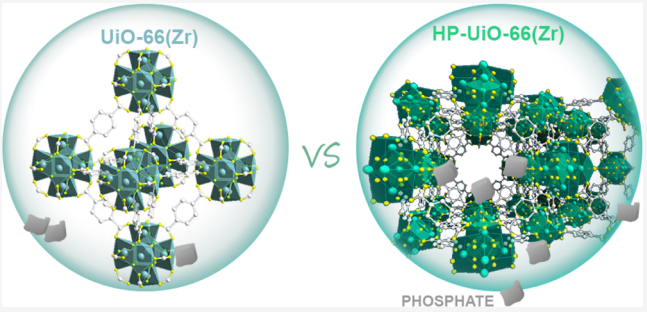

KEYWORDS: *metal−organic frameworks, monocarboxylic acids, defect chemistry, hierarchical pores, phosphate removal*

INTRODUCTION

Metal−organic frameworks (MOFs) are organic−inorganic hybrid crystalline porous materials composed of a regular array of metal ions (or clusters) linked by organic ligands.[1−3] The intriguing properties of MOFs, including permanent porosity, high chemical stability, and excellent tunability,[4,5] have rendered them as highly attractive sorbents toward environmental remediation.[6,7] Compared with traditional adsorbents, such as activated carbon and metal oxides, MOFs exhibit highly tunable structures, compositions, and pore sizes (at atomic and molecular levels).[8−10] However, most reported MOFs are highly microporous (e.g., pore size <2 nm),[11] which may block the molecules of interest (e.g., tetrahedral phosphate anions) from entering the cavities within the frameworks.[12] For instance, the phosphate adsorption capacity of UiO-66(Zr) has been reported to be rather limited (74.5 mg P/g).[13]

One potential solution to increase the phosphate adsorption capacity of MOFs is to fabricate hierarchical porous MOFs (HP-MOFs).[14] For instance, Deng et al. reported that the pore aperture of MOF-74 could be expanded from the microporous to mesoporous range by extending the number of phenylene ring links.[15] This facilitated the utilization of inaccessible active sites within the micropores. Another promising strategy to improve the phosphate sorption performance is by introducing additional bonding sites via defect engineering.[16,17] Defects are often associated with unoccupied coordination sites at metal clusters of MOFs, which tend to be exposed on the introduced pores of MOFs. By understanding and controlling the type and level of defects within MOFs, the adsorption performance can be enhanced through the introduction of enlarged pores (e.g., mesopores) and abundant sorption active sites (e.g., unsaturated coordination centers).[18] Currently, template-assisted routes are commonly adopted to fabricate HP-MOFs,[19] which incorporate sacrificial templates (e.g., surfactants,[20] nanoparticles,[2] and metal−organic assemblers[21]) during the fabrication of MOFs, and enlarged cavities can be created following removal of the template. This strategy introduces engineered mesopores

Received: March 16, 2021
Revised: September 10, 2021
Accepted: September 13, 2021
Published: September 23, 2021

https://doi.org/10.1021/acs.est.1c01723
Environ. Sci. Technol. 2021, 55, 13209−13218

together with crystal defects within specific frameworks; however, the template removal step may cause collapse of the frameworks. Another alternative template-based strategy takes advantage of the tunability of MOFs to introduce labile chemical bonds (e.g., using modulators as terminal ligands to coordinate with the metal clusters) to synthesize robust HP-MOFs.[22,23] The introduced chemical bonds can be easily removed by a subsequent activation process to create unsaturated coordination centers inside the HP-MOFs. Recently, Zhou and coworkers have reported such a strategy to construct HP-PCN-250 with abundant surface and internal mesopores.[11] However, very few reports are available on the defect engineering of HP-MOFs to tune their structure−property relationship toward adsorption applications.

Herein, an advanced strategy is adopted to introduce both defects and hierarchical pores in UiO-66 and to fine-tune its adsorption behavior toward phosphate. Several monocarboxylic acids of varying chain lengths (XA, with high pK_a) are selected to precoordinate with Zr−O clusters, which can be partially replaced with insufficient ligands (H_2BDC, with low pK_a), followed by further assembly into the UiO-66(Zr)-XA nanoparticles. Increased defect density and expanded pores can be introduced in the preformed MOFs by removing the fatty acid linkers during the activation process. We have chosen phosphate as the target aqueous contaminant to evaluate the efficacy of the as-fabricated HP-UiO-66(Zr) due to its hazardous nature toward aquatic ecosystems and drinking water supply. HP-UiO-66(Zr) with stoichiometrically deficient BDC linkers is hypothesized to (i) dramatically improve the phosphate mass transport, (ii) afford additional unsaturated sorption sites, and (iii) mitigate the secondary contamination owing to the replacement of carboxylic acid ligands during phosphate uptake. To the best of our knowledge, this work is among the very few studies undertaken to explore the defect engineering of HP-UiO-66 to boost its phosphate sorption performance. The findings of this study can provide mechanistic insights into the defect engineering of HP-MOFs for environmental applications.

MATERIALS AND METHODS

Chemicals. Dimethylformamide (DMF), hydrochloric acid (HCl, 36−38%), methanol (MeOH), sodium sulfate (Na_2SO_4), sodium nitrate ($NaNO_3$), sodium chloride (NaCl), sodium phosphate dibasic dodecahydrate ($Na_2HPO_4{\cdot}12H_2O$), sodium bicarbonate ($NaHCO_3$), sodium hydroxide (NaOH), potassium selenate (K_2SeO_4), activated alumina (Al_2O_3, diameter: 6−9 mm), polystyrene anion exchanger D201 (diameter: 0.6−0.9 mm), zirconia (ZrO_2) (diameter: 200 nm), and iron oxide (Fe_2O_3) (diameter: 200 nm) were supplied by Sinopharm Chemical Reagent Co., Ltd. (China). Formic acid (HCOOH), butyric acid ($C_4H_8O_2$), octanoic acid ($C_8H_{16}O_2$), palmitic acid ($C_{16}H_{32}O_2$), 1,4-benzenedicarboxylic acid (BDC), humic acid (HA), and zirconium(IV) chloride ($ZrCl_4$) were purchased from Sigma-Aldrich. All aqueous solutions were prepared with ultrapure water (18.25 MΩ cm) produced from a Milli-Q Direct 8 purification system (Millipore, USA).

Synthesis of Hierarchically Porous UiO-66(Zr). The synthetic procedures of hierarchically porous UiO-66(Zr)-XA (HP-UiO-66(Zr)-XA) were similar to those of UiO-66(Zr) (details are available in the Supporting Information, Section S1) except by adding desired aliphatic monocarboxylic acids (e.g., formic acid (FA), butyric acid (BA), octanoic acid (OA), and palmitic acid) into the DMF solution in advance of BDC at a fixed molar ratio (Zr/BDC/monocarboxylic acid = 1:0.5:25). The as-obtained white precipitate was rinsed with DMF three times to remove the remnant monocarboxylic acid. To further remove the monocarboxylate acids, the sample was placed into 80 mL of solution of 1.25% HCl and 98.75% DMF at 90 °C for 12 h, and this step was repeated three times. The final product was collected by centrifugation, washed sequentially with DMF and methanol, and then subjected to solvent exchange by immersing the product in methanol twice, each time for 24 h. Finally, the product was dried at 75 °C for 12 h under vacuum.

Batch Sorption Experiments. For isotherm experiments, 10 mg of the sample was introduced into a 150 mL flask containing 100 mL of phosphate solution (3−30 mg P/L) and shaken for 24 h with a speed of 200 rpm to achieve sorption equilibrium at 25 °C and pH 6.5. The isotherm curves were fitted with Langmuir and Freundlich models (Supporting Information, Section S1). The kinetic experiments were conducted under the same conditions, except that the concentration of phosphate was 3 mg P/L and shaking time was reduced to 240 min. The kinetic curves were fitted with Weber−Morris intraparticle diffusion models (Supporting Information, Section S1). After centrifugation (8500 rpm, 10 min), the supernatant was filtered using a 0.22 μm Millipore filter. The residual phosphate concentration was quantified with an ICS 5000 ion chromatograph (Thermo Fisher Scientific, Waltham) equipped with an Ion Pac AS11-HC column (250 mm × 4 mm).

To examine the regeneration efficacy of HP-UiO-66(Zr)-OA, 10 mg of the exhausted sample was regenerated by chemical washing with 100 mL of NaOH solution (0.01 mol/L) at 25 °C and stirring at 600 rpm for 8 h. Then, the regenerated adsorbents were dried in a vacuum oven at 120 °C for 12 h before the next cycle. All sorption experiments were performed in triplicate to ensure good reproducibility. The impacts of common competitive anions (e.g., SO_4^{2-}, Cl^-, and NO_3^-) and natural organic matter (NOM, e.g., HA) on the phosphate sorption performance of HP-UiO-66(Zr)-OA, Al_2O_3, and polystyrene anion exchanger D201 were comparatively investigated (details are provided in Table S1).

Column Experiments. Fixed-bed column experiments were performed in a glass column ($<l>$ = 65 mm and $<d>$ = 8 mm). The column was filled with a certain amount of adsorbent, and the bed volume was 4.5 mL. The empty bed contact time was 3 min as controlled by a peristaltic pump (DH1766A-1, China). The samples were subjected to regeneration by chemical washing with 0.01 mol/L NaOH solution at 25 °C followed by subsequent washing with deionized water until the effluent was neutral. The Zr content in the effluent was determined by the inductively coupled plasma−optical emission spectrometry (ICP-OES) technique to examine the loss of Zr during the column test.

Characterization. The physicochemical properties of the as-designed materials were analyzed by X-ray diffraction (XRD), field emission scanning electron microscopy (SEM), transmission electron microscopy (TEM), X-ray photoelectron spectroscopy (XPS), X-ray absorption spectroscopy (XAS), Brunauer−Emmett−Teller (BET) specific surface area, dynamic light scattering (DLS), photoluminescence, ^{1}H nuclear magnetic resonance (^{1}H/NMR), electron paramagnetic resonance (EPR) spectroscopy, an elemental analyzer, thermogravimetric analyses (TGA), and differential scanning calorimetry (DSC). In addition, the used samples after phosphate uptake were further characterized by Fourier transform infrared (FTIR) spectroscopy, XPS, XRD, and EPR techniques. Further details of

https://doi.org/10.1021/acs.est.1c01723
Environ. Sci. Technol. 2021, 55, 13209−13218

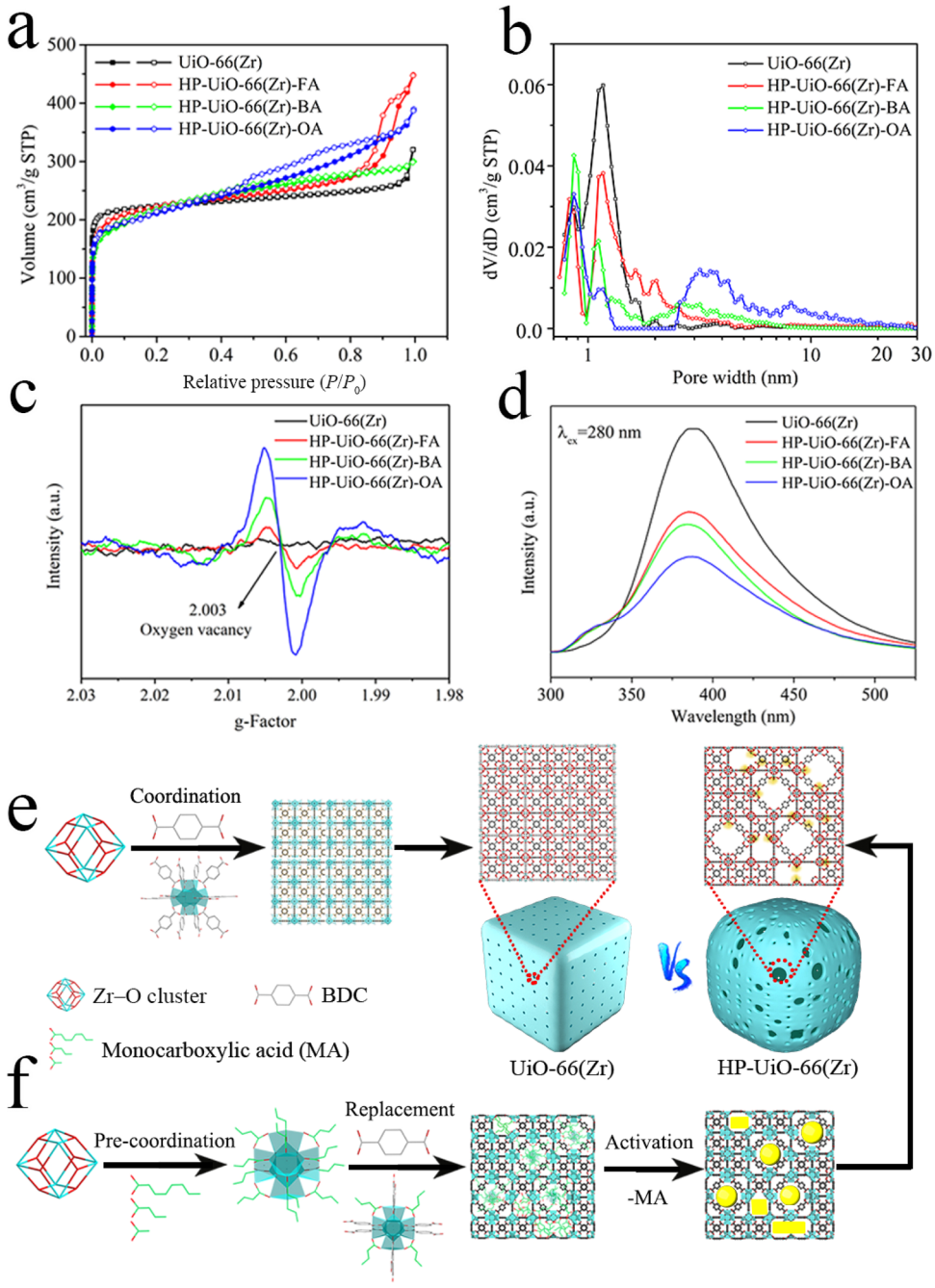

Figure 1. (a) N_2 adsorption−desorption isotherms of UiO-66(Zr) and various HP-UiO-66(Zr)-XA samples obtained with different aliphatic acids (filled data markers represent adsorption, and open data markers represent desorption) and (b) corresponding pore size distribution. (c) EPR spectra and (d) fluorescence emission spectra of UiO-66(Zr) and various HP-UiO-66(Zr)-XA samples. Formation schematic of (e) pristine UiO-66(Zr) and (f) defective HP-UiO-66(Zr).

the characterization techniques and density functional theory (DFT) calculations are provided in the Supporting Information.

RESULTS AND DISCUSSION

Defective HP-UiO-66(Zr) Evolution. SEM and powder X-ray diffraction (PXRD) were employed to characterize the as-prepared HP-UiO-66(Zr) derivatives. With the increasing alkyl chain length, the surface morphologies of these samples become rough, and the particle size exhibits a volcanic-type variation tendency (Figure S1a−e), and the defect content is gradually increased (Figure S1f). Furthermore, the main peaks in the FTIR spectra of HP-UiO-66(Zr)-XA are consistent with those of UiO-66(Zr), indicating that the original UiO-66 structure is still maintained after the modulation of monocarboxylic acid (Figure S2). N_2 adsorption−desorption isotherms and the corresponding pore size distribution plots were used to analyze the effect of the carbon chain length of the monocarboxylic acids on the pore dimensions of HP-UiO-66(Zr)-XA. As shown in Figure 1a, the pristine UiO-66(Zr) shows a Type I isotherm, which is typical of a microporous structure. The HP-UiO-66(Zr)-FA sample also displays a large uptake of N_2 gas in the low-pressure range, which supports the presence of micropores. Another uptake of N_2 gas with a hysteresis loop in the pressure range of 0.8−1.0 is attributed to the presence of macropores,

https://doi.org/10.1021/acs.est.1c01723
Environ. Sci. Technol. 2021, 55, 13209−13218

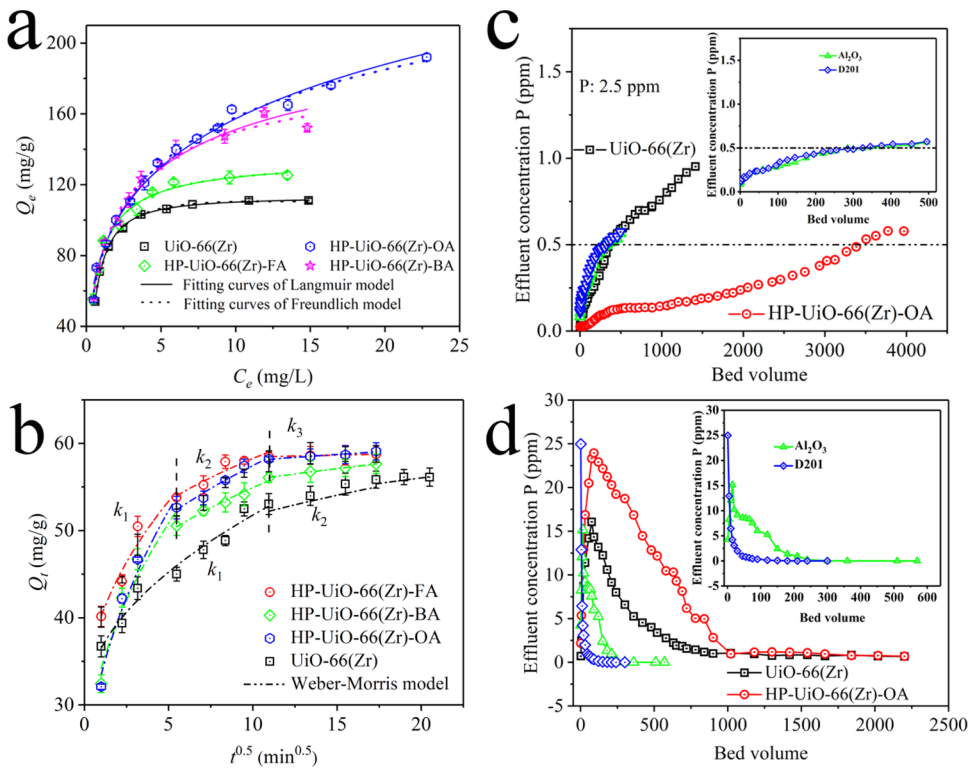

Figure 2. (a) Phosphate adsorption isotherms and (b) kinetic curves fitting with Weber and Morris intraparticle diffusion models of UiO-66(Zr) and HP-UiO-66(Zr)-XA. (c) Breakthrough curves of UiO-66(Zr), HP-UiO-66(Zr)-OA, Al_2O_3, and polystyrene anion exchanger D201. (d) In situ regeneration curves of UiO-66(Zr) and HP-UiO-66(Zr)-OA. Experimental conditions: sorbent dose = 50 mg, [P] = 2.5 mg/L, initial pH = 6.5, T = 25 °C, and bed volume: 4.5 mL.

which do not affect the pore size distribution in micro- and mesopore ranges (Figure 1b). More interestingly, both HP-UiO-66(Zr)-BA and HP-UiO-66(Zr)-OA exhibit mesopores ranging from 2.0 to 7.0 nm and 2.5 to 16 nm, respectively. From Figure 1b, it is revealed that the size of the mesopores increases with increasing carbon chain length of aliphatic acids. In addition, the pore volume of mesopores increases from 38.8 to 64.3% as the chain length of the fatty acids is increased from C1 to C8 (Table S2).

EPR and fluorescence spectroscopy were employed to explore the effects of elongated monocarboxylic acids on the structural characteristics of UiO-66(Zr) and its derivatives. As shown in Figure 1c, the EPR spectrum of the UiO-66(Zr) shows a negligible peak, which may be attributed to inherent defects. Once monocarboxylic acids are introduced, the spectra show a distinct peak at g = 2.003, indicating the existence of a significant amount of uncoupled Zr(IV) centers, which serve as defects in the frameworks.[24−26] Additionally, the level of defects increases considerably with the increasing chain length (from FA to OA), most likely due to the steric hindrance of the precoordinated fatty chains. Likewise, the fluorescence spectra also confirm the presence of defects (Figure 1d). The intensity of fluorescence signals (ex/em = 280 nm/395 nm) follows the order of UiO-66(Zr) > HP-UiO-66(Zr)-FA > HP-UiO-66(Zr)-BA > HP-UiO-66(Zr)-OA. This phenomenon can be explained by the fact that the fluorescence intensity can be mediated by the coordination numbers of Zr−O clusters and BDC in the UiO-66(Zr).[27] Combining the above results, Zr atoms in pristine UiO-66 are coordinately saturated with ligands (BDC), resulting in the formation of uniform micropores (Figure 1e). When sufficient aliphatic acids (C1−C8) were added in advance, their elongated alkyl chains with a higher pK_a can be regarded as capping agents to precoordinate with Zr atoms in Zr−O clusters. This is because the increased alkyl chain may hamper the monocarboxylic replacement by the insufficient BDC and coordination with the adjacent Zr(IV) via steric hindrance, thus leading to larger pore dimensions and unsaturated sites upon the eventual activation process (Figure 1f). Based on these results, it is confirmed that porous HP-UiO-66(Zr)-XA with extended pore diameters (0.7−15 nm) and many coordinative unsaturated active centers (Zr(IV)) are successfully synthesized.

Tunable Phosphate Adsorption by HP-UiO-66(Zr)-XA. Figure 2a displays the phosphate adsorption capacities of the tested adsorbents as a function of phosphate concentration. The isotherms fit well with both Langmuir and Freundlich models (Langmuir R^2 > 0.97; Freundlich R^2 > 0.97), indicating that the adsorption process originates from an integrated monolayer and chemisorption.[28,29] The maximum phosphate adsorption capacity (q_m) estimated by the Langmuir model follows an order of HP-UiO-66(Zr)-OA (186.6 mg P/g) > HP-UiO-66(Zr)-BA (80.2 mg P/g) > HP-UiO-66(Zr)-FA (45.3 mg P/g) > UiO-66(Zr) (37.7 mg P/g) (Table S3). These results suggest that the phosphate adsorption capacity is more strongly influenced by the defect level of HP-MOFs rather than their surface areas (Figure 1c; Table S2). The q_m value of HP-UiO-66(Zr)-OA for phosphate removal is comparable or higher than that of previously reported MOFs, ZrO_2, and hierarchical zeolite-based adsorbents (Table S4).[30−32] Moreover, the phosphate sorption capacity of HP-UiO-66(Zr)-XA before activation is decreased with the increasing chain length and follows the sequence UiO-66(Zr) (38.1 mg P/g) > UiO-66(Zr)-

https://doi.org/10.1021/acs.est.1c01723
Environ. Sci. Technol. 2021, 55, 13209−13218

FA (38.7 mg P/g) > UiO-66(Zr)-BA (34.2 mg P/g) > UiO-66(Zr)-OA (30.5 mg P/g) (Figure S3). This trend can be attributed to the large number of monocarboxylic acids remaining in the nonactivated samples (^{1}H/NMR analyses, Figures S4 and S5), which not only occupy the coordinatively unsaturated Zr atoms but also deteriorate the mass-transport kinetics.

The phosphate adsorption kinetics of UiO-66(Zr) and HP-UiO-66(Zr)-XA were also compared. The Weber−Morris intraparticle diffusion model was employed to investigate the intraparticle diffusion process. As presented in Figure 2b, compared to the pristine UiO-66(Zr), the enhanced liquid film diffusion rate (k_1) of HP-UiO-66(Zr)-XA (Table S5) may be caused by the increased zeta potential on its surface (Figure S6). More importantly, the internal diffusion rate (k_2) is increased with the increase of the alkyl chain length and follows the order HP-UiO-66(Zr)-OA (6.19 mg/g·min$^{0.5}$) > HP-UiO-66(Zr)-BA (5.47 mg/g·min$^{0.5}$) > HP-UiO-66(Zr)-FA (5.18 mg/g·min$^{0.5}$) > UiO-66(Zr) (3.22 mg/g·min$^{0.5}$). Owing to the enlarged pore dimensions, the time required to achieve the phosphate sorption equilibrium is shortened from 180 min (UiO-66(Zr)) to 120 min (HP-UiO-66(Zr)-XA), revealing that the generated hierarchical pores can dramatically improve the mass transport of phosphate within HP-UiO-66(Zr). Based on the adsorption isotherms and kinetics, the HP-UiO-66(Zr)-OA sample has the highest adsorption capacity and the fastest intraparticle diffusion rate at the same molar ratio of Zr/BDC/XA (1:0.5:25). DLS results reveal that there are no obvious correlations between the MOF particle size and the phosphate sorption capacity as well as the removal kinetics (Figure S7). Given that BDC is responsible for the generation of the hierarchical porous structure, the effect of the BDC concentration on the formed MOFs was evaluated. The phosphate adsorption performance of HP-UiO-66(Zr)-OA (Y) prepared with different BDC stoichiometric ratios (Y = 0.3, 0.5, 0.8) is presented in Figure S8 and Table S6. The crystallinity of the sample obtained with a BDC/Zr ratio of 0.3 is lower than that obtained with other ratios (Figure S9). In addition, the pore size increases from 7.5 to 12 nm as the BDC/Zr ratio is increased from 0.3 to 0.8. These results clearly indicate that the formation of mesopores and the low surface area are caused by the reduced amount of BDC ligand (Figure S10). The phosphate sorption capacity presents a volcanic-type trend and follows the sequence HP-UiO-66(Zr)-OA (0.5, 186.6 mg P/g) > HP-UiO-66(Zr)-OA (0.8, 60.9 mg P/g) > HP-UiO-66(Zr)-OA (0.3, 58.0 mg P/g) > UiO-66(Zr) (1.0, 37.7 mg P/g). Based on this trend, it is clear that the ideal phosphate adsorbent is obtained at an optimal Zr/BDC/OA ratio of 1:0.5:25, which is used as the default parameter for HP-UiO-66(Zr)-OA hereafter, unless suggested otherwise.

A fixed-bed filtration device was employed to further exemplify the practicality of HP-UiO-66(Zr)-OA for phosphate adsorption. The results suggest that the effective treatment volume of HP-UiO-66(Zr)-OA (50 mg) is ∼3400 BV, one order of magnitude higher than that of UiO-66(Zr) (50 mg, ∼450 BV), activated Al_2O_3 (50 mg, ∼302 BV), polystyrene anion exchanger D201 (50 mg, ∼371 BV), ZrO_2 (100 mg, ∼1890 BV), and Fe_2O_3 (100 mg, ∼2560 BV) under similar conditions (Figures 2c and S11). Subsequently, these samples were subjected to in situ regeneration by washing with 0.01 M NaOH solution at 20 BV/h. The HP-UiO-66(Zr)-OA sample exhibits excellent regeneration performance (up to 95% of the phosphate is desorbed) as seen in Figure 2d. Furthermore, the Zr loss of the HP-UiO-66(Zr)-OA sample during the column tests is measured to be 3.5 μg/L Zr based on the effluent collected at the 7500 BV (Figure S12). In addition, batch experiments of sorption/desorption were performed to evaluate the reusability of HP-UiO-66(Zr)-OA, as shown in Figure S13. Impressively, the regenerated HP-UiO-66(Zr)-OA can maintain almost 90% of the initial phosphate removal efficiency after three consecutive sorption/desorption experiments. In addition, EPR spectra of the regenerated HP-UiO-66(Zr)-XA(P) sample show the reappearance of uncoupled Zr(IV) (g = 2.003, Figure S14), suggesting that phosphate is mainly coordinated with the unsaturated Zr−O clusters within HP-UiO-66(Zr)-XA. The specific surface area of HP-UiO-66(Zr)-OA after phosphate sorption and regeneration is slightly decreased to 505 m^2/g. However, their mesopores remain intact (Figure S15). Overall, these results confirm the excellent robustness and high sorption/desorption performance of HP-UiO-66(Zr)-OA. Therefore, it can be envisaged for the long-term phosphate adsorption applications.

Mechanism of Phosphate Removal Using HP-UiO-66(Zr)-OA. TEM and the corresponding elemental mapping reveal the uniform distribution of P throughout the HP-UiO-66(Zr)-OA sample. The Zr K-edge X-ray absorption near-edge structure (XANES) analysis indicates the existence of a strong interaction between phosphate and HP-UiO-66(Zr)-OA (Figure S16). Notably, the characteristic peaks in the range of 900−1200 cm^{-1}, corresponding to −OH binding vibrations involved in the formation of Zr_6-clusters in UiO-66(Zr) and HP-UiO-66(Zr)-OA, become weaker after phosphate uptake (Figure S17, FTIR spectra). Concurrently, the broad and intense vibration bands at 1150 and 1076, 990, and 545 cm^{-1} are clearly observed in HP-UiO-66(Zr)-OA-(P), which can be attributed to the formation of P═O, P−OH, and O−P−O bonds.[33] This indicates the plausible complexation between Zr−OH groups in HP-UiO-66(Zr)-OA and phosphate via Zr−O−P coordination bonds.[34] In addition, an obvious absorption peak at 430 cm^{-1} (μ_3-OH vibration of the solvent H_2O molecules) is observed in HP-UiO-66(Zr)-OA(P),[35] indicating that the hydroxyl groups originated from the Zr−O cluster and solvent H_2O may participate in the phosphate adsorption. XPS analysis was further performed to unveil the key mechanism driving the host (UiO-66(Zr) or HP-UiO-66(Zr)-OA)−guest (phosphate) interactions (Figures S18 and S19). Compared with the reference spectrum of KH_2PO_4 (about 134.0 eV), the intensity of the P 2p peak in HP-UiO-66(Zr)-OA is strong and blue shifted to 133.8 eV, thus indicating the occurrence of chemical bonding between phosphate and HP-UiO-66(Zr)-OA (Figure S18).[36] More importantly, a prominent binding energy signal appears at 191.3 eV in the Zr 3d spectrum of HP-UiO-66(Zr)-OA-(P), which is attributed to the electronic interactions between the Zr atom and phosphate (Figure S19b).[37] In the O 1 s XPS peak, the Zr−OH peak (531.8 eV) of UiO-66(Zr) and HP-UiO-66(Zr)-OA after phosphate adsorption can be deconvoluted into P−OH (533.2 eV), Zr−O−P, and P═O (531.5 eV) (Figures S19c and S19d),[27] revealing that the hydroxyl groups play a key role in the phosphate adsorption process via strong complexation. Meanwhile, the area ratios of P−Zr (134.5 eV) to P−O (133.6 eV) in the UiO-66(Zr)-(P) and HP-UiO-66(Zr)-OA-(P) samples are 0.2 and 0.12 (Figures S19e and S19f),[38,39] respectively, indicating that the sequestration of phosphate by the coordinatively unsaturated Zr center in HP-UiO-66(Zr)-OA via Zr−P bonds is unlikely to be the dominant mechanism for the phosphate sorption. The large number of Zr−OH groups mainly originates from the defects

https://doi.org/10.1021/acs.est.1c01723
Environ. Sci. Technol. 2021, 55, 13209−13218

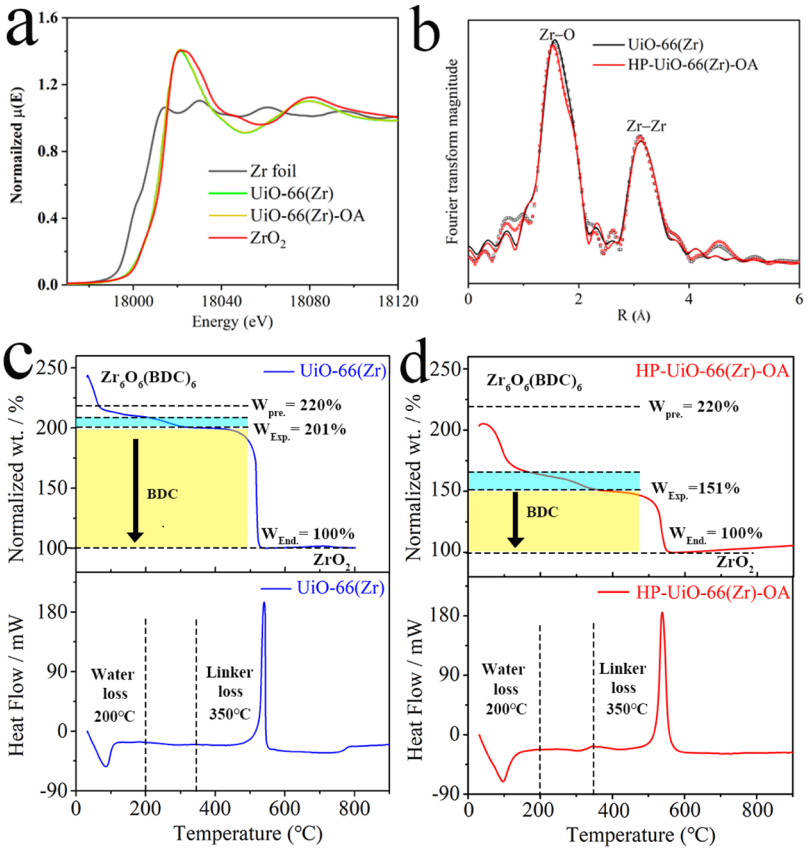

Figure 3. (a) XANES and (b) EXAFS spectra of the Zr K-edge in UiO-66(Zr) and HP-UiO-66(Zr)-OA. Experimental and calculated curves are displayed as black/red lines and black/red open circles, respectively. (c,d) TGA-DSC thermograms of UiO-66(Zr) and HP-UiO-66(Zr)-OA.

present in Zr−O clusters;[18] thus, terminal ligands (OH^-/H_2O) are required to compensate for the defects in the HP-UiO-66(Zr)-OA framework.

To further ascertain the experimental findings, three complementary characterization techniques were employed to identify the defect-compensating ligands of the prepared HP-MOF samples. First, previous studies[23,40] have suggested that the defect-compensating ligands mainly originated from chloride ($ZrCl_4$),[41] OH^-/H_2O (environment or solvent),[42] or monocarboxylates (the added modulators, octoate).[43] Nevertheless, in this study, both chloride and monocarboxylates can be ruled out on the basis of ^{1}H/NMR (Figures S4 and S5) results. A series of measurements was performed to investigate the possible introduction of OH^-/H_2O for the defect formation in the HP-UiO-66(Zr)-OA. To identify this, the contents of Zr, C, H, and O in these samples (mass percent) were analyzed by the ICP-OES technique and elemental analyzer (Table S7). Based on the chemical formula of pristine UiO-66(Zr) ($Zr_6O_4(OH)_4(BDC)_6$), the mean coordination number of BDC linkers in HP-UiO-66(Zr)-OA is 2.4, which is lower than that of the as-prepared UiO-66(Zr) (5.04) and pristine UiO-66(Zr) (6). The minimum number of BDC linkers required to form a continuous three-dimensional UiO-66 network is 3. In other words, each cluster is coordinated by at least six linkers (3 × 2). This finding indicates the presence of more missing cluster defects in HP-UiO-66(Zr)-OA, consistent with the pore size distribution analysis. Furthermore, XAS was used to ascertain the oxidative states and coordination environment of Zr in UiO-66(Zr) and HP-UiO-66(Zr)-OA. As shown in Figure 3a, after modulation by OA, the Zr oxidation state does not significantly change. The EXAFS spectra reveal the local coordination environment around the Zr atoms, showing two dominant peaks at 1.7 and 3.1 Å, attributed to Zr−O and Zr−Zr, respectively (Figure 3b, Tables S8−S12, and Figures S20 and S21). No significant differences are observed in the peak position between UiO-66(Zr) and HP-UiO-66(Zr)-OA; however, the intensity and symmetry of the Zr−O peak are decreased in the latter as compared to UiO-66(Zr). This evolution may be attributed to the introduction of (OH^-/H_2O) into the framework.

With this in mind, TGA-DSC was used to qualitatively characterize the thermal decomposition behaviors of the samples. Three well-resolved weight loss regions are observed in the TGA curves (end weight normalized to 100%) (Figure 3c,d). The observed weight loss steps are assigned to (i) physical absorption (30−100 °C);[44] (ii) dehydroxylation of the Zr_6 cornerstones (200−350 °C);[45] and (iii) framework decomposition (420−560 °C) accompanied by an intense exothermic peak in the DSC thermogram.[46] The mass losses of hydroxyl groups in UiO-66(Zr) and HP-UiO-66(Zr)-OA are 6 and 13% in the temperature region of 200−350 °C, respectively (detailed discussion on the TGA results is given in the Supporting Information, Section S1). Meanwhile, the coordination numbers of Zr−OC in UiO-66(Zr) and HP-UiO-66(Zr)-OA are 5.1 and 2.5, respectively, which are in good agreement with the elemental analysis results. Based on these results, the defect-induced ligand-compensation (−OH) model is suitable to describe the phosphate adsorption behavior of HP-UiO-66(Zr)-OA, as the Zr−OH (−OH, originating from the solvent) can be swiftly replaced by the more electronegative phosphate ions.

https://doi.org/10.1021/acs.est.1c01723
Environ. Sci. Technol. 2021, 55, 13209−13218

DFT Calculations. To further elucidate the role of defects (i.e., linker missing and cluster missing) in HP-UiO-66(Zr)-XA toward phosphate adsorption, the possible interaction scenarios between the perfect unit cell (Figure 4a), missing linker unit cell

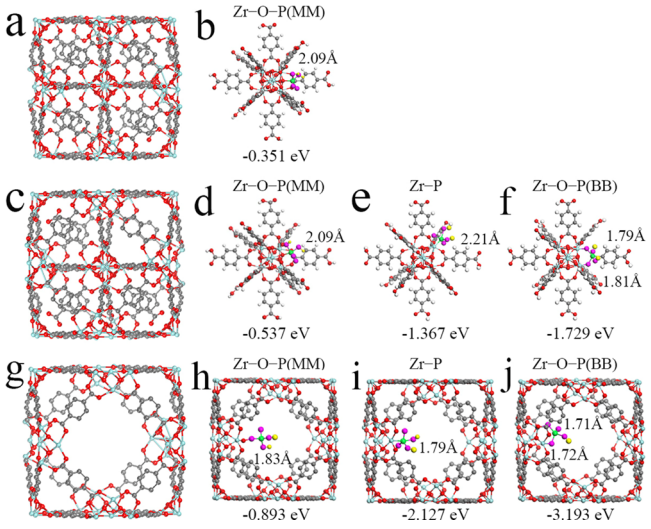

Figure 4. DFT calculation models for different structures: (a) Perfect UiO-66(Zr) unit cell, (b) Zr–O–P (MM) coordination between perfect UiO-66(Zr) and $H_2PO_4^-$, (c) missing linker defect of the UiO-66(Zr) unit cell, (d–f) Zr–O–P (MM), Zr–P, and Zr–O–P (BB) coordination between the missing linker defect and phosphate ($H_2PO_4^-$), (g) missing cluster defect of the UiO-66(Zr) unit cell, (h–j) Zr–O–P (MM), Zr–P, and Zr–O–P (BB) coordination between the missing cluster defect and $H_2PO_4^-$ (prasine for P, cyan for Zr, and red for O from the Zr–O cluster, amaranth for O from phosphate, gray for C, white for H from UiO-66(Zr), and yellow for H from $H_2PO_4^-$).

(Figure 4c), and the missing cluster unit cell of UiO-66(Zr) (Figure 4g) with phosphate ($H_2PO_4^-$, as the computational model) were investigated at the molecular level through DFT calculations. The adsorption energy of Zr–O–P (MM, mononuclear monodentate, Figure 4b) coordination is −0.351 eV, indicating a spontaneous adsorption process. After modulation with monocarboxylic acids, the optimal configurations between the missing linker defects and $H_2PO_4^-$ are shown in Figure 4d–f. Apart from the Zr–O–P (MM) coordination (adsorption energy: −0.537 eV), other sorption pathways are observed as well (e.g., Zr–P and Zr–O–P (BB, binuclear bidentate)). The Zr–P coordination reveals that these unsaturated Zr atoms (caused by the missing linker) are capable of directly interacting with $H_2PO_4^-$ to form an inner spherical complex (Figure 4e, the locally magnified image is shown in Figure S22). The defect-compensating ligands (−OH) are replaced by $H_2PO_4^-$ ions to coordinate with residual defective Zr atoms, leading to the Zr–O–P (BB) coordination interactions (Figure 4f, the locally magnified image is given in Figure S22). These results indicate that the missing linker defects not only provide additional sorption sites but also reduce the adsorption energy of the original active sites. For the missing cluster defects, a large space is available in the unit cell due to the absence of the Zr–O cluster, which accelerates the transport of $H_2PO_4^-$ toward sorption active sites. This is supported by the kinetic studies and the selenate adsorption experiments. The experimental results show that HP-UiO-66(Zr)-OA with the largest pore dimension has the fastest intraparticle diffusion kinetics among the prepared HP-UiO-66(Zr) samples (Figure 2b; Table S5). In addition, HP-UiO-66(Zr)-OA demonstrates a higher selenate (SeO_4^{2-}) removal efficiency (11.5%) in the presence of sulfate (SO_4^{2-}) than pristine UiO-66(Zr) (5.0%) (Figure S23). In addition, similar sorption pathways are observed with the missing linker defects toward phosphate adsorption (Figure 4h–j). More importantly, the corresponding adsorption energies in the missing cluster and missing linker defects are lower than those in the perfect UiO-66(Zr) unit cell (Figure 4). These results clearly reveal that the created defects in HP-UiO-66(Zr)-XA play a significant role in boosting the adsorption affinity toward phosphate by forming newly dominant adsorption sites and strengthening the mass transport of phosphate within HP-UiO-66(Zr)-XA to reduce the time required to achieve the phosphate sorption equilibrium (Figure 2b). These results confirm the excellent phosphate performance of HP-UiO-66(Zr)-OA with elevated defect levels, which are in good agreement with both experimental and recent research findings (Figures 1 and 2, and Table S3).[47]

Environmental Implications. Given the complex nature of actual environments, solution pH, coexisting anions, and NOM may significantly deteriorate the phosphate uptake efficacy. As shown in Figure S24, the HP-UiO-66(Zr)-OA sample exhibits a superior phosphate removal efficiency (>90%) to UiO-66(Zr) in the pH range of 2.0–6.0. Further increasing the solution pH to alkaline conditions leads to a clear decline in the phosphate removal efficiency to 60% at pH = 8.0. The observed phenomenon is expected as the point-of-zero-charge of HP-UiO-66(Zr)-OA is 7.8, and the pK_a values of phosphate molecules are 2.1, 7.2, and 12.3, respectively.[29] Thus, HP-UiO-66(Zr)-OA becomes negatively charged under alkaline conditions and exhibits strong repulsion toward anionic phosphate molecules. A similar trend is observed for UiO-66(Zr). The robustness of UiO-66(Zr) and HP-UiO-66(Zr)-OA was further examined by detecting the Zr leaching rate as a function of pH (Figure S25). Both HP-UiO-66(Zr)-OA and UiO-66(Zr) show <2% of Zr loss under acidic and neutral conditions. In addition, no obvious changes are identified in the XRD patterns of UiO-66(Zr) and HP-UiO-66(Zr)-OA before and after phosphate sorption, further confirming the robustness of these materials (Figure S26). To further explore the selectivity of HP-UiO-66(Zr)-OA for phosphate removal in practical environments, the phosphate sorption behavior in the presence of several common anions (e.g., Cl^- (3.32 Å), NO_3^- (3.35 Å), and SO_4^{2-} (3.79 Å)) and NOM (e.g., HA) was examined as well. As displayed in Figure 5, the distribution coefficients (K_d, details are given in the Supporting Information, Section S1) of HP-UiO-

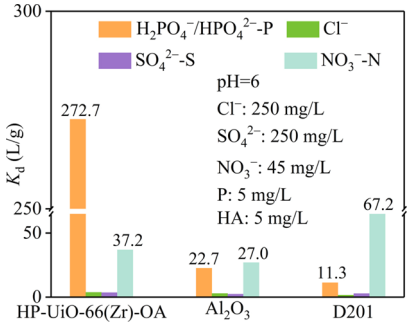

Figure 5. Impact of competitive anions and NOM on the phosphate uptake by HP-UiO-66(Zr)-OA, Al_2O_3, and polystyrene anion exchanger D201.

https://doi.org/10.1021/acs.est.1c01723
Environ. Sci. Technol. 2021, 55, 13209−13218

66(Zr)-OA, Al_2O_3, and D-201 toward phosphate follow the sequence HP-UiO-66(Zr)-OA (272.7 L/g) > Al_2O_3 (22.7 L/g) > D-201 (11.3 L/g). In addition, the K_d value of HP-UiO-66(Zr)-OA in the mixtures of common anions and NOM follows the order $HPO_4^{2-}/H_2PO_4^-$ (272.7 L/g) > NO_3^- (37.2 L/g) > Cl^- (3.8 L/g) > SO_4^{2-} (3.6 L/g). Generally, a high K_d value indicates a high ion uptake by the sorbent.[29] These results demonstrate that HP-UiO-66(Zr)-OA has a higher selectivity toward phosphate ions in the simulated wastewater relative to Al_2O_3 and polystyrene anion exchanger D-201. This phenomenon may be attributed to the predominant phosphate sorption mechanism in HP-UiO-66(OA), which originates from the formation of Zr−O−P bonds. Therefore, these common coexisting anions, such as Cl^-, SO_4^{2-}, and NO_3^-, exert insignificant inhibition on the phosphate uptake.[48]

In conclusion, an array of defect-induced hierarchical porous UiO-66(Zr) derivatives have been rationally designed by employing different monocarboxylic acid modulators. The pore dimension and phosphate sorption performance of the developed UiO-66 materials can be fine-tuned by controlling the type and level of defects. Among the as-prepared HP-UiO-66(Zr)-XA adsorbents, HP-UiO-66(Zr)-OA exhibits the best performance with porous nanospherical morphology, large volume percentage of mesopores (64%), broad size distribution of mesopores (2.5−16 nm), maximum adsorption capacity (186.6 mg P/g), desirable stability (less than 2% of Zr leaching under acidic and neutral conditions), and excellent phosphate selectivity in simulated wastewater (pH = 6). This study provides new insights into the phosphate sorption mechanism of defective MOFs with hierarchical porous structures. The DFT results reveal the significant role of the created defects in HP-UiO-66(Zr)-XA for boosting the adsorption affinity toward phosphate by forming newly active bonding sites and strengthening the mass transfer of phosphate in HP-UiO-66(Zr)-XA interior. The findings in this study will provide useful guidance for designing defect-rich MOF-based adsorbents with high adsorption performance for practical adsorption applications.

■ ASSOCIATED CONTENT

Supporting Information

The Supporting Information is available free of charge at https://pubs.acs.org/doi/10.1021/acs.est.1c01723.

(Section S1) Experimental section; (Sections S2 and S3) characterizations, (Section S4) theoretical calculations; (Tables S1−S12) quality of simulated water, BET/BJH results, maximum adsorption capacity for phosphate, comparison of the phosphate adsorption capacity, phosphate adsorption kinetics, elemental mass percentage, and EXAFS fitting parameters; and (Figures S1−S26) SEM images, PXRD patterns, ^{1}H/NMR spectra, zeta potential curves, N_2 adsorption−desorption isotherms, Zr dissolution, TEM image, XPS spectra, SEM-EDS spectra, DFT calculation models, stability, repeatability, pH, and EXAFS spectrum of HP-UiO-66(Zr)-OA (PDF)

■ AUTHOR INFORMATION

Corresponding Authors

Yanbiao Liu − *Textile Pollution Controlling Engineering Center of Ministry of Environmental Protection, College of Environmental Science and Engineering, Donghua University, Shanghai 201620, China;* orcid.org/0000-0001-8404-3806; Email: yanbiaoliu@dhu.edu.cn

Yusuf Valentino Kaneti − *Australian Institute for Bioengineering and Nanotechnology (AIBN), The University of Queensland, Brisbane, Queensland 4072, Australia;* orcid.org/0000-0003-2433-7305; Email: v.kaneti@uq.edu.au

Chong-Chen Wang − *Beijing Key Laboratory of Functional Materials for Building Structure and Environment Remediation, Beijing University of Civil Engineering and Architecture, Beijing 100044, China;* orcid.org/0000-0001-6033-7076; Email: wangchongchen@bucea.edu.cn

Authors

Mohua Li − *Textile Pollution Controlling Engineering Center of Ministry of Environmental Protection, College of Environmental Science and Engineering, Donghua University, Shanghai 201620, China*

Fang Li − *Textile Pollution Controlling Engineering Center of Ministry of Environmental Protection, College of Environmental Science and Engineering, Donghua University, Shanghai 201620, China*

Chensi Shen − *Textile Pollution Controlling Engineering Center of Ministry of Environmental Protection, College of Environmental Science and Engineering, Donghua University, Shanghai 201620, China;* orcid.org/0000-0003-4459-566X

Yusuke Yamauchi − *Australian Institute for Bioengineering and Nanotechnology (AIBN), The University of Queensland, Brisbane, Queensland 4072, Australia; JST-ERATO Yamauchi Materials Space-Tectonics Project and International Center for Materials Nanoarchitectonics (WPI-MANA), National Institute for Materials Science (NIMS), Ibaraki 305-0044, Japan;* orcid.org/0000-0001-7854-927X

Brian Yuliarto − *Advanced Functional Materials Laboratory, Department of Engineering Physics and Research Center for Nanosciences and Nanotechnology (RCNN), Institute of Technology Bandung, Bandung 40132, Indonesia;* orcid.org/0000-0003-0662-7923

Bo Chen − *Department of Chemistry, City University of Hong Kong, Hong Kong 999077, China;* orcid.org/0000-0001-6743-9251

Complete contact information is available at: https://pubs.acs.org/10.1021/acs.est.1c01723

Notes

The authors declare no competing financial interest.

■ ACKNOWLEDGMENTS

This work was supported by the National Natural Science Foundation of China (51878023), Beijing Natural Science Foundation (8202016), Great Wall Scholars Training Program Project of Beijing Municipality Universities (CIT&TCD20180323), Beijing Talent Project (2019A22), the Fundamental Research Funds for the Central Universities and Graduate Student Innovation Fund of Donghua University (CUSF-DH-D-2020072), and the JST-ERATO Yamauchi Materials Space-Tectonics Project (JPMJER2003). This work was partly performed at the Queensland node of the Australian National Fabrication Facility (ANFF), a company established under the National Collaborative Research Infrastructure Strategy to provide nano- and micro-fabrication facilities for Australian researchers.

REFERENCES

(1) Dhaka, S.; Kumar, R.; Deep, A.; Kurade, M. B.; Ji, S.; Jeon, B. Metal-Organic Frameworks (MOFs) for the Removal of Emerging Contaminants from Aquatic Environments. *Coord. Chem. Rev.* **2019**, *380*, 330−352.

(2) Zhang, W. N.; Liu, Y. Y.; Lu, G.; Wang, Y.; Li, S. Z.; Cui, C. L.; Wu, J.; Xu, Z. L.; Tian, D. B.; Huang, W.; Ducheneu, J. S.; Wei, W. D.; Chen, H. Y.; Yang, Y. H.; Huo, F. W. Mesoporous Metal−Organic Frameworks with Size, Shape, and Space-Distribution-Controlled Pore Structure. *Adv. Mater.* **2015**, *27*, 2923−2929.

(3) Qin, Y.; Han, X.; Li, Y.; Han, A.; Liu, W.; Xu, H.; Liu, J. Hollow Mesoporous Metal−Organic Frameworks with Enhanced Diffusion for Highly Efficient Catalysis. *ACS Catal.* **2020**, *10*, 5973−5978.

(4) Wang, C. C.; Li, J. R.; Lv, X. L.; Zhang, Y. Q.; Guo, G. S. Photocatalytic Organic Pollutants Degradation in Metal−Organic Frameworks. *Environ. Eng. Sci.* **2014**, *7*, 2831−2867.

(5) Chen, Y.; Du, Y.; Liu, P.; Yang, J.; Li, L.; Li, J. Removal of Ammonia Emissions *via* Reversible Structural Transformation in M(BDC) (M = Cu, Zn, Cd) Metal−Organic Frameworks. *Environ. Sci. Technol.* **2020**, *54*, 3636−3642.

(6) Li, Y.; Yang, Z.; Wang, Y.; Bai, Z.; Zheng, T.; Dai, X.; Liu, S.; Gui, D.; Liu, W.; Chen, M.; Chen, L.; Diwu, J.; Zhu, L.; Zhou, R.; Chai, Z.; Albrecht-Schmitt, T. E.; Wang, S. A Mesoporous Cationic Thorium-Organic Framework that Rapidly Traps Anionic Persistent Organic Pollutants. *Nat. Commun.* **2017**, *8*, 1354.

(7) Liu, K.; Zhang, S.; Hu, X.; Zhang, K.; Roy, A.; Yu, G. Understanding the Adsorption of PFOA on MIL-101(Cr)-Based Anionic-Exchange Metal-Organic Frameworks: Comparing DFT Calculations with Aqueous Sorption Experiments. *Environ. Sci. Technol.* **2015**, *49*, 8657−8665.

(8) Thorarinsdottir, A. E.; Harris, T. D. Metal−Organic Framework Magnets. *Chem. Rev.* **2020**, *120*, 8716−8789.

(9) Kirchon, A.; Feng, L.; Drake, H. F.; Joseph, E. A.; Zhou, H. From Fundamentals to Applications: A Toolbox for Robust and Multifunctional MOF Materials. *Chem. Soc. Rev.* **2018**, *47*, 8611−8638.

(10) Hassan, M. H.; Stanton, R.; Secora, J.; Trivedi, D. J.; Andreescu, S. Ultrafast Removal of Phosphate from Eutrophic Waters using a Cerium-Based Metal-Organic Framework. *ACS Appl. Mater. Interfaces* **2020**, *12*, 52788−52796.

(11) Kirchon, A.; Li, J.; Xia, F.; Day, G. S.; Becker, B.; Chen, W.; Sue, H.; Fang, Y.; Zhou, H. Modulation versus Templating: Fine-Tuning of Hierarchally Porous PCN-250 using Fatty Acids To Engineer Guest Adsorption. *Angew. Chem., Int. Ed.* **2019**, *58*, 12425−12430.

(12) Chen, H.; Snurr, R. Q. Understanding the Loading Dependence of Adsorbate Diffusivities in Hierarchical Metal-Organic Frameworks. *Langmuir* **2020**, *36*, 1372−1378.

(13) Guan, T.; Li, X.; Fang, W.; Wu, D. Efficient Removal of Phosphate from Acidified Urine Using UiO-66 Metal−Organic Frameworks with Varying Functional Groups. *Appl. Surf. Sci.* **2020**, *501*, No. 144074.

(14) Cirujano, F. G.; Martin, N.; Wee, L. H. Design of Hierarchical Architectures in Metal-Oganic Frameworks for Catalysis and Adsorption. *Chem. Mater.* **2020**, *32*, 10268−10295.

(15) Deng, H.; Grunder, S.; Cordova, K. E.; Valente, C.; Furukawa, H.; Hmadeh, M.; Gandara, F.; Whalley, A. C.; Liu, Z.; Asahina, S.; Kazumori, H.; O'Keeffe, M.; Terasaki, O.; Stoddart, J. F.; Yaghi, O. M. Large-Pore Apertures in a Series of Metal-Organic Frameworks. *Science* **2012**, *336*, 1018−1023.

(16) Chong, S.; Thiele, G.; Kim, J. Excavating Hidden Adsorption Sites in Metal−Organic Frameworks Using Rational Defect Engineering. *Nat. Commun.* **2017**, *8*, 1539.

(17) Svane, K. L.; Bristow, J. K.; Gale, J. D.; Walsh, A. Vacancy Defect Configurations in the Metal−Organic Framework UiO-66: Energetics and Electronic Structure. *J. Mater. Chem. A* **2018**, *6*, 8507−8513.

(18) Dissegna, S.; Epp, K.; Heinz, W. R.; Kieslich, G.; Fischer, R. A. Defective Metal−Organic Frameworks. *Adv. Mater.* **2018**, *30*, No. 1704501.

(19) Zhou, K.; Zhang, C.; Xiong, Z. Y.; Chen, H. Y.; Li, T.; Ding, G. L.; Yang, B. D.; Liao, Q. F.; Zhou, Y.; Han, S. T. Template-Directed Growth of Hierarchical MOF Hybrid Arrays for Tactile Sensor. *Adv. Funct. Mater.* **2020**, *30*, No. 2001296.

(20) Zhao, Y. J.; Zhang, J. L.; Han, B. X.; Song, J. L.; Li, J. S.; Wang, Q. A. Metal−Organic Framework Nanospheres with Well-Ordered Mesopores Synthesized in an Ionic Liquid/CO_2/Surfactant System. *Angew. Chem., Int. Ed.* **2011**, *50*, 636−639.

(21) Huang, H. L.; Li, J. R.; Wang, K. K.; Han, T. T.; Tong, M. M.; Li, L. S.; Xie, Y. B.; Yang, Q. Y.; Liu, D. H.; Zhong, C. L. An *In Situ* Self-Assembly Template Strategy for the Preparation of Hierarchical-Pore Metal−Organic Frameworks. *Nat. Commun.* **2015**, *6*, 8847.

(22) Cai, G.; Jiang, H. L. A Modulator-Induced Defect-Formation Strategy to Hierarchically Porous Metal−Organic Frameworks with High Stability. *Angew. Chem., Int. Ed.* **2017**, *56*, 563−567.

(23) Vermoortele, F.; Bueken, B.; Le Bars, G.; Van de Voorde, B.; Vandichel, M.; Houthoofd, K.; Vimont, A.; Daturi, M.; Waroquier, M.; Van Speybroeck, V.; Kirschhock, C.; De Vos, D. E. Synthesis Modulation as a Tool to Increase the Catalytic Activity Of Metal−Organic Frameworks: The Unique Case of UiO-66(Zr). *J. Am. Chem. Soc.* **2013**, *135*, 11465−11468.

(24) Zhang, G.; Ji, Q.; Zhang, K.; Chen, Y.; Li, Z.; Liu, H.; Li, J.; Qu, J. Triggering Surface Oxygen Vacancies on Atomic Layered Molybdenum Dioxide for a Low Energy Consumption Path toward Nitrogen Fixation. *Nano Energy* **2019**, *59*, 10−16.

(25) Ji, Q. Q.; Bi, L.; Zhang, J. T.; Cao, H. J.; Zhao, X. S. The Role of Oxygen Vacancies of ABO(3) Perovskite Oxides in the Oxygen Reduction Reaction. *Environ. Eng. Sci.* **2020**, *13*, 1408−1428.

(26) Ren, Y.; Liu, Y.; Liu, F.; Li, F.; Shen, C.; Wu, Z. Extremely Efficient Electro-Fenton-Like Sb(III) Detoxification Using Nanoscale Ti-Ce Binary Oxide: An Effective Design to Boost Catalytic Activity *Via* Non-Radical Pathway. *Chin. Chem. Lett.* **2021**, 2519.

(27) Yang, J.; Dai, Y.; Zhu, X.; Wang, Z.; Li, Y.; Zhuang, Q.; Shi, J.; Gu, J. Metal−Organic Frameworks with Inherent Recognition Sites for Selective Phosphate Sensing through Their Coordination-Induced Fluorescence Enhancement Effect. *J. Mater. Chem. A* **2015**, *3*, 7445−7452.

(28) Liu, Y. B.; Gao, G. D.; Vecitis, C. D. Prospects of an Electroactive Carbon Nanotube Membrane toward Environmental Applications. *Acc. Chem. Res.* **2020**, *53*, 2892−2902.

(29) Wu, B.; Wan, J.; Zhang, Y.; Pan, B.; Lo, I. M. C. Selective Phosphate Removal from Water and Wastewater using Sorption: Process Fundamentals and Removal Mechanisms. *Environ. Sci. Technol.* **2020**, *54*, 50−66.

(30) Liu, R. T.; Chi, L. N.; Wang, X. Z.; Wang, Y.; Sui, Y. M.; Xie, T. T.; Arandiyan, H. Effective and Selective Adsorption of Phosphate from Aqueous Solution *via* Trivalent-Metals-Based Amino-MIL-101 MOFs. *Chem. Eng. J.* **2019**, *357*, 159−168.

(31) Shi, W.; Fu, Y.; Jiang, W.; Ye, Y.; Kang, J.; Liu, D.; Ren, Y.; Li, D.; Luo, C.; Xu, Z. Enhanced Phosphate Removal by Zeolite Loaded with Mg-Al-La Ternary (Hydr)oxides from Aqueous Solutions: Performance and Mechanism. *Chem. Eng. J.* **2019**, *357*, 33−44.

(32) Su, Y.; Cui, H.; Li, Q.; Gao, S.; Shang, J. K. Strong Adsorption of Phosphate by Amorphous Zirconium Oxide Nanoparticles. *Water Res.* **2013**, *47*, 5018−5026.

(33) Elzinga, E. J.; Sparks, D. L. Phosphate Adsorption onto Hematite: An in Situ ATR-FTIR Investigation of the Effects of pH and Loading Level on the Mode of Phosphate Surface Complexation. *J. Colloid Interface Sci.* **2007**, *308*, 53−70.

(34) Qiu, H.; Ye, M.; Zeng, Q.; Li, W.; Fortner, J.; Liu, L.; Yang, L. Fabrication of Agricultural Waste Supported UiO-66 Nanoparticles with High Utilization in Phosphate Removal from Water. *Chem. Eng. J.* **2019**, *360*, 621−630.

(35) Meng, F.; Zhang, S.; Ma, L.; Zhang, W.; Li, M.; Wu, T.; Li, H.; Zhang, T.; Lu, X.; Huo, F.; Lu, J. Construction of Hierarchically Porous Nanoparticles@Metal−Organic Frameworks Composites by Inherent Defects for the Enhancement of Catalytic Efficiency. *Adv. Mater.* **2018**, *30*, No. 1803263.

(36) Wu, B.; Lo, I. M. C. Surface Functional Group Engineering of CeO_2 Particles for Enhanced Phosphate Adsorption. *Environ. Sci. Technol.* **2020**, *54*, 4601−4608.

https://doi.org/10.1021/acs.est.1c01723
Environ. Sci. Technol. 2021, 55, 13209−13218

(37) Colon, J. L.; Thakur, D. S.; Yang, C. Y.; Clearfield, A.; Martin, C. R. X-Ray Photoelectron-Spectroscopy and Catalytic Activity of Alpha-Zirconium Phosphate and Zirconium-Phosphate Sulfophenylphosphonate. *J. Catal.* **1990**, *124*, 148−159.
(38) Jiang, J.; Kim, D. L.; Dorji, P.; Phuntsho, S.; Hong, S.; Shon, H. K. Phosphorus Removal Mechanisms from Domestic Wastewater by Membrane Capacitive Deionization and System Optimization for Enhanced Phosphate Removal. *Process. Saf. Environ.* **2019**, *126*, 44−52.
(39) Arfelli, M.; Mattogno, G.; Ferragina, C.; Massucci, M. A. XPS Characterization of γ-Zirconium Phosphate and of Some of Its Intercalation Compounds. A Comparison with the α-Zirconium Phosphate Analogues. *J. Inclusion Phenom. Mol. Recognit. Chem.* **1991**, *15*, 15−27.
(40) Shearer, G. C.; Chavan, S.; Ethiraj, J.; Vitillo, J. G.; Svelle, S.; Olsbye, U.; Lamberti, C.; Bordiga, S.; Lillerud, K. P. Tuned to Perfection: Ironing out the Defects in Metal−Organic Framework UiO-66. *Chem. Mater.* **2014**, *26*, 4068−4071.
(41) Bara, D.; Wilson, C.; Mörtel, M.; Khusniyarov, M. M.; Ling, S.; Slater, B.; Sproules, S.; Forgan, R. S. Kinetic Control of Interpenetration in Fe−Biphenyl-4,4′-dicarboxylate Metal−Organic Frameworks by Coordination and Oxidation Modulation. *J. Am. Chem. Soc.* **2019**, *141*, 8346−8357.
(42) Liu, C.; Zhang, A. Y.; Pei, D. N.; Yu, H. Q. Efficient Electrochemical Reduction of Nitrobenzene by Defect Engineered TiO_{2-X} Single Crystals. *Environ. Sci. Technol.* **2016**, *50*, 5234−5242.
(43) Ntep, T. J. M. M.; Reinsch, H.; Schluesener, C.; Goldman, A.; Breitzke, H.; Moll, B.; Schmolke, L.; Buntkowsky, G.; Janiak, C. Acetylenedicarboxylate and In Situ Generated Chlorofumarate-Based Hafnium(IV)-Metal-Organic Frameworks: Synthesis, Structure, and Sorption Properties. *Inorg. Chem.* **2019**, *58*, 10965−10973.
(44) Kandiah, M.; Nilsen, M. H.; Usseglio, S.; Jakobsen, S.; Olsbye, U.; Tilset, M.; Larabi, C.; Quadrelli, E. A.; Bonino, F.; Lillerud, K. P. Synthesis and Stability of Tagged UiO-66 Zr-MOFs. *Chem. Mater.* **2010**, *22*, 6632−6640.
(45) Shearer, G. C.; Forselv, S.; Chavan, S.; Bordiga, S.; Mathisen, K.; Bjorgen, M.; Svelle, S.; Lillerud, K. P. In Situ Infrared Spectroscopic and Gravimetric Characterisation of the Solvent Removal and Dehydroxylation of the Metal Organic Frameworks UiO-66 and UiO-67. *Top. Catal.* **2013**, *56*, 770−782.
(46) Valenzano, L.; Civalleri, B.; Chavan, S.; Bordiga, S.; Nilsen, M. H.; Jakobsen, S.; Lillerud, K. P.; Lamberti, C. Disclosing the Complex Structure of UiO-66 Metal Organic Framework: A Synergic Combination of Experiment and Theory. *Chem. Mater.* **2011**, *23*, 1700−1718.
(47) Stanton, R.; Trivedi, D. J. Influence of Defects and Linker Exchange on Removal of Phosphate Using MOFs with the Node Structure $M_6(OH)_4(O)_4$ for M = Hf, Zr, or Ce. *Chem. Mater.* **2021**, *33*, 5730−5737.
(48) Schmidtchen, F. P. Hosting Anions. The Energetic Perspective. *Chem. Soc. Rev.* **2010**, *39*, 3916−3935.

https://doi.org/10.1021/acs.est.1c01723
Environ. Sci. Technol. 2021, 55, 13209−13218